

# X-ray Solar Event Identification using Convolutional Neural Networks

Ted Grosson, Cody Meng, Preston Tracy, Jackson White

Advisor: Chris Tunnell — Rice University

Submitted May 12, 2021

## Introduction

Solar events—such as flares, prominences, and their associated coronal mass ejections—can lead to detrimental effects on Earth systems by disrupting electronics and communication systems, particularly in satellites with limited protection from Earth’s magnetic field. Large flares can produce streams of ionized particles intense enough to harm or kill unprotected astronauts in orbiting spacecraft. Even larger flares, such as the 1859 Carrington Event famously strong enough to set fire to telegraph wires [1], pose existential threats to modern society with the potential to irreparably damage large swaths of the power grid, disable aircraft navigational and computer systems, and disrupt radio communications or military early-warning systems [2]. Given the immediacy of these threats, understanding solar events and space weather is a major scientific priority, with three U.S. organizations (the Space Weather Prediction Center, the Air Force Weather Agency, and NASA) dedicated to researching space weather systems.

From a scientific perspective, the physical mechanisms underlying solar events are not precisely understood [3]. Solar flares are generally classified by a peak in total solar intensity at a particular wavelength rather than by imaging of the structure of a flare. We wanted to investigate whether we could detect or classify solar events using images of the Sun rather than by simply measuring total intensity. If different types of flares carry unique observational signatures held within images of the Sun, this could hint at specific physical mechanisms underlying flares of varying types. In order to find whether these signatures of solar events exist, we use convolutional neural networks trained on thousands of multi-wavelength Extreme-Ultraviolet solar images alongside space weather reports of solar events. While the black-box nature of machine learning prevents us from obtaining a detailed understanding of the exact underlying trends, deep-learning neural nets are unparalleled at finding patterns in data. Thus, they are ideal for determining whether these patterns occur at all solar events.

## Background

Solar flares are highly energetic events of localized (though not small, up to tens of thousands of kilometers across) increased intensity on the Sun, releasing up to  $10^{25}$  Joules over a time period ranging from milliseconds to over an hour [3]. This intensity can be seen across many wavelengths, including X-ray to radio, as illustrated in Figure 14. For comparison, Figure 15 shows the Sun without an active event. Flares tend to be associated with groups of sunspots—localized regions of cooler material and strong magnetic fields—and are often accompanied by the ejection of charged particles, called a coronal mass ejection. The precise cause of solar flares remains uncertain, but the leading theory is that energy is suddenly released from the strong magnetic field in sunspots through a process called “reconnection” [3]. This occurs when a magnetic field loop “breaks” and

“reconnects” in a more stable path, releasing most of the energy stored in the loop. Although the amount of energy predicted to be stored in these loops is consistent with the energy of the flares themselves, it is still unclear how the energy conversion occurs [3].

Previous studies using AIA data tend to focus on characterizing the dynamics [4][5] or structure [6] of particular events. This is due to the large quantity of high quality images provided by the AIA, allowing extremely detailed studies of solar features. In contrast, our project focuses on the detection of events as a whole without detailed study of flare structure. Most studies also combine AIA data with data from the Helioseismic and Magnetic Imager (HMI), which maps out the magnetic field on the solar surface [4][5]. Since solar flares are directly related to changes in the solar magnetic field, HMI data provides a simple method for searching for events. However, we would like to discover whether identification can be achieved through purely visual means, so we are not using magnetic field data from the HMI.

There have been some successful prior efforts to predict the solar flares using machine learning based on changes in the Sun’s magnetic field [7]; however, because solar flare events are associated with changes in the Sun’s magnetic field, previous studies have not established whether they can be predicted via purely imaging techniques. The success of this project at identifying solar X-ray flares using Extreme Ultraviolet images suggests that these images could in fact be used for predicting solar events.

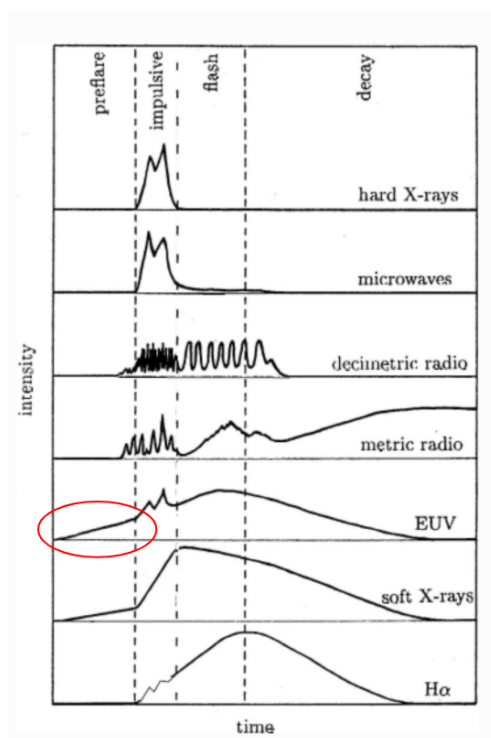


Figure 1: Typical Intensity vs. Time curves of X-ray flares in various wavebands [8]. The waveband most relevant to our work is the EUV (Extreme Ultraviolet) spanning 100 Å to 1240 Å, where most of our observations lie. This suggests that our images should carry clear signatures of X-ray flares. Also worth noting in this figure is the longer buildup in EUV intensity in the preflare stage, circled in red. Images from the preflare stage will show an increase in EUV intensity before the impulsive peaks in the hard X-ray wavelengths, forecasting the more harmful X-ray emission.

Solar flares that peak in one wavelength are expected to have broad spectra which are visible in additional wavelengths [8]. As shown in Figure 1, X-ray flares are expected to also be visible in the EUV wavelengths that we have access to from the AIA observatory. These EUV companions should also be present at increased intensity levels both before and after the X-ray flares appear on the Sun, as shown by the large temporal spread of the EUV distribution. This is an indicator that it may be possible to not only identify X-ray solar flares with AIA data, but also predict their occurrence before they are visible in the X-ray wavelengths.

## Objectives

We apply machine learning image classification techniques to historical high-resolution multi-waveband solar images from the Atmospheric Imaging Assembly (AIA) in order to train a set of convolutional neural networks to identify X-ray solar events from rapid-cadence, live images of the Sun obtained by the AIA. As such, our primary objective is to produce a binary classifier capable of identifying X-ray solar events with high accuracy using only AIA images.

## Data Science Pipeline

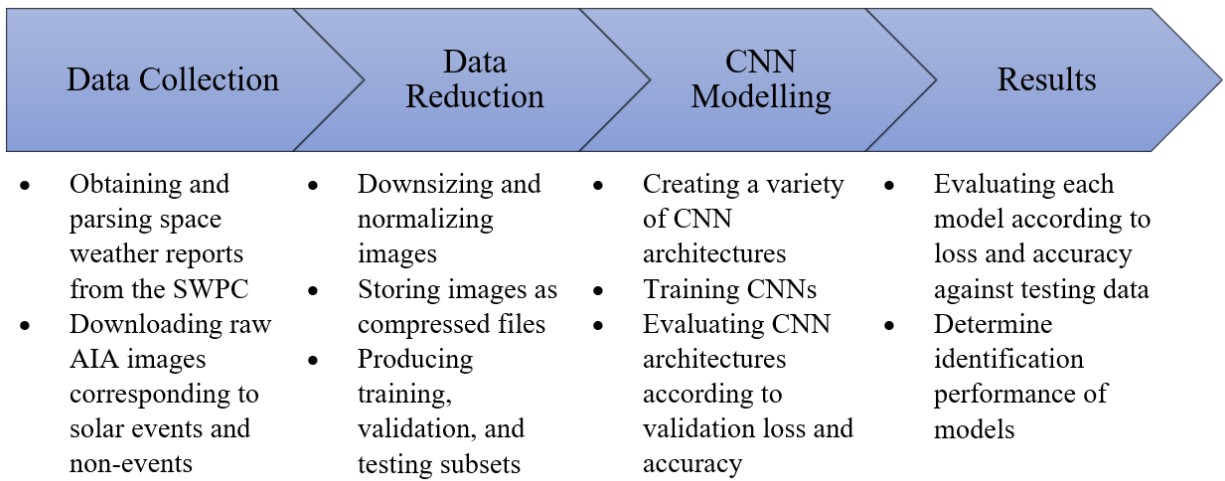


Figure 2: This figure outlines the steps in our data science pipeline. The data collection step involves the processes relating to obtaining and downloading raw data from our different sources (SWPC and AIA). The data reduction step involves the “wrangling” of the data, or the process of turning the raw data into a form that is usable as inputs for our CNNs. This step involves downsizing and normalizing the raw images and storing the images as files that can easily be loaded by the CNN. The modelling step involves the creation and training of the various CNN architectures that were tested. Finally, the results section involves the process of determining the optimal CNN structure based on accuracy and loss metrics.

## Data & Data Exploration

In this project we use two primary datasets. The first is over a decade of high-resolution, 16 megapixel images of the Sun in 10 ultraviolet and optical wavelengths taken at an approximately 12-second cadence by the Atmospheric Imaging Assembly (AIA), a solar imager located aboard the Solar Dynamics Observatory (SDO), a satellite orbiting the Earth dedicated to providing constant measurements of the Sun in order to understand solar events [9]. The second is a database of space weather reports from the Space Weather Prediction Center (SWPC), a part of the National Weather Service (NWS) run by the National Oceanic and Atmospheric Administration (NOAA). These space weather reports catalog all detected solar events with a time, date, duration, and classification. Events are reported to the SWPC by several different ground- and space-based detectors.



Figure 3: An artists rendering of the Solar Dynamics Observatory in orbit. The Atmospheric Imaging Assembly include the four telescopes shown facing the Sun in this image. [10]

### AIA Observations

The AIA takes observations at ten different wavelengths, summarized in Table 1, each probing different layers of the Sun. The AIA has been observing the Sun since 2010, observing at  $4500 \text{ \AA}$  once per hour, at  $1600$  and  $1700 \text{ \AA}$  every 24 seconds ( $0.04166 \text{ Hz}$ ), and at the remaining wavelengths every 12 seconds ( $0.0833 \text{ Hz}$ ) [11]. The images are stored as  $4096 \times 4096$  pixel FITS (Flexible Image Transport System [12]) files, a pixel array format where each pixel represents the flux captured by its corresponding pixel on the AIA camera. FITS files also contain headers including relevant information such as exposure time and the time of the observation. These files can be queried and

downloaded within Python using version 2.1.4 [13] of the SUNPY open source software package [14]. Using SUNPY, we can select images based on their observation time and wavelength filter, allowing easy data access for events listed in the space weather reports.

The different wavelengths observed by AIA were chosen to examine specific portions of the Sun’s surface or atmosphere. Each of these wavelengths are centered on a different emission line to examine the features visible at the temperature of the emission line. The EUV wavelengths observe extremely hot temperatures, and are centered on different iron ions, ranging from Fe IX (171 Å) to Fe XXIII (131 Å), and observing temperatures from  $6 \times 10^4$  K (304 Å) to  $2 \times 10^7$  K (193 Å) [15]. The 1700 Å and 4500 Å wavelengths show continuum images of the Sun in the UV and optical, respectively. The 1600 Å wavelength examines the transition region between the chromosphere and the corona. The 304 Å wavelength also examines the transition region, as well as the chromosphere. The 171 Å wavelength shows the “quiet” (low magnetic activity) corona and coronal loops, and the 193 Å examines a hotter region of the corona, as well as the hotter material in solar flares. The 211 Å and 335 Å wavelengths both examine the hot, magnetically active regions of the corona. Finally, the 94 Å and 131 Å wavelengths both examine flaring regions, with wavelengths centered at different temperatures [16]. The temperature coverage provided by these wavelengths allows for a more complete reconstruction of thermal structure than previous missions [11].

AIA Filter Details

Wavelength (Å)	Emission Source	Region of Atmosphere	$\log_{10}(\text{Temp})$ (K)
4500	Continuum	Photosphere	3.7
1700	Continuum	Photosphere	3.7
1600	C IV + Continuum	Photosphere / Transition Region	4.7
335	Fe XVI	Flaring Regions	6.8
304	He II	Chromosphere / Transition Region	5.8
211	Fe XIV	Active-Region Corona	6.3
193	Fe XII, XXIV	Corona / Hot Flare Plasma	6.1, 7.3
171	Fe IX	Corona / Transition Region	5.0
131	Fe VIII, XX, XXIII	Flaring Regions	5.6, 7.0, 7.2
94	Fe XVIII	Flaring Regions	6.8

Table 1: The wavelengths observed by the AIA, the primary source of emission (continuum or spectral line source) at each wavelength, the approximate layer of the Sun probed at this wavelength, and the  $\log_{10}$  of the temperature, in Kelvin, of this layer. [11]

## SWPC Space Weather Reports

The second dataset, constituting thousands of space weather reports, are created once per day by the Space Weather Prediction Center (SWPC) and can contain many different types of space weather events, including X-ray events (XRA), optical flares (FLA), radio sweep bursts (RSP), and fixed-frequency radio bursts (RBR). These reports have been catalogued since 1997, so we have

reports corresponding to all AIA data. A sample report from 2015 is depicted in Figure 5. The entire collection of reports is only 18 MB in storage size and is stored in easy-to-parse text files, so no major concerns arose when using this dataset.

The reports are compiled from several different detectors maintained by NOAA, including two Geostationary Operational Environmental Satellites (GOES) and many ground-based detectors located around the planet. These detectors mostly measure flux of either electromagnetic radiation or charged particles, and alerts are sent to the SWPC based on threshold detection methods [17].

Of the 15 classifications of solar events listed in Figure 4, we primarily look at four due to their frequency. FLA events are flares on the solar surface peaking in the optical observed via  $H\alpha$  emission, XRA events are spikes in solar X-ray flux, RBR events are narrow-band (ie. fixed frequency) radio bursts, and RSP events are radio bursts sweeping through a range of radio frequencies over the duration of the event [18]. The remaining 11 categories of solar event do not appear in large enough numbers to justify their focus. In addition, these small samples may not be large enough to reliably train machine learning algorithms, especially given our emphasis on binary classification techniques.

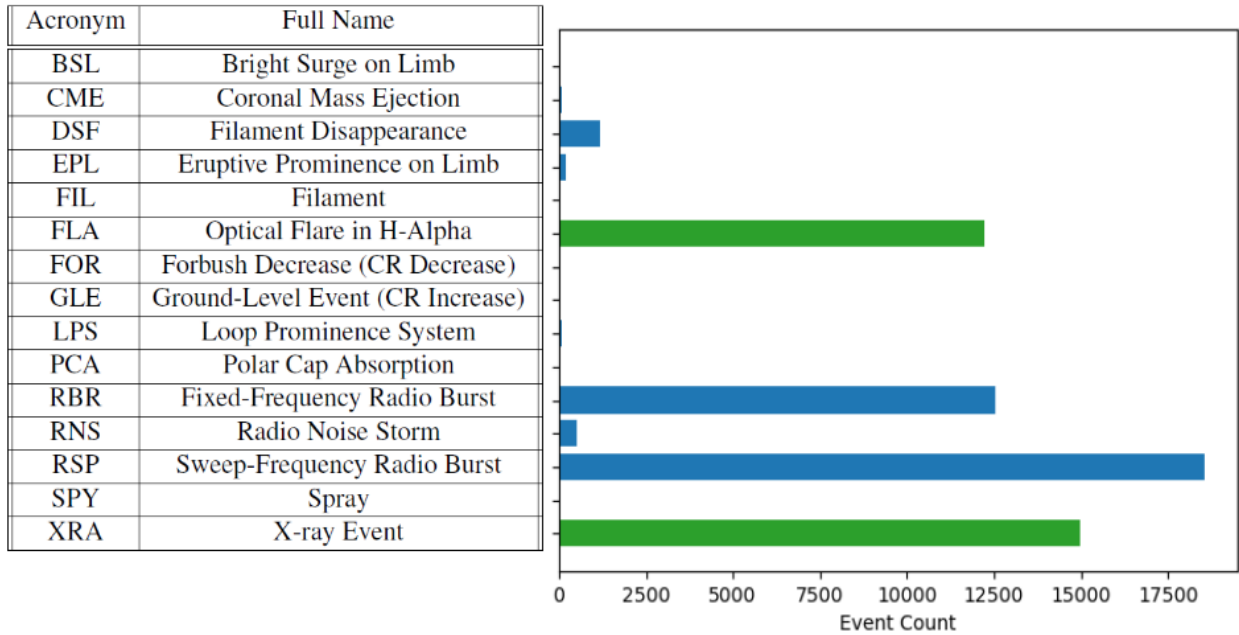


Figure 4: Total number of SWPC space weather events observed since 2010, grouped by event type, with the types used in this study highlighted in green. Of the 15 event types shown, only four types have large enough sample sizes to train a precise neural network—XRA, FLA, RSP, and RBR. XRA events are sharp increases in X-ray solar intensity above typical background levels due to a flare or prominence. FLA events are solar flares with intensity peaking in the optical. RSP and RBR events are bursts at radio wavelengths, with RBR (Radio Burst) events peaking at a fixed wavelength over time and RSP (Radio Sweep) events peaking at fluctuating wavelengths over time. Each of these peaks can range from factors of a few up to roughly 6 orders of magnitude above background intensity levels. At this point, we are focusing on the XRA and FLA events (highlighted in green) due to the fact that their principal wavelengths are close to the ultraviolet range of our images, unlike the radio bursts.



```

:Product: 20150617events.txt
:Created: 2015 Jun 18 2127 UT
:Date: 2015 06 17
# Prepared by the U.S. Dept. of Commerce, NOAA, Space Weather Prediction Center
# Please send comments and suggestions to SWPC.Webmaster@noaa.gov
#
# Missing data: ////
# Updated every 5 minutes.
#
# Edited Events for 2015 Jun 17
#
#Event      Begin      Max      End  Obs  Q  Type  Loc/Frq  Particulars      Reg#
#-----
3910        0040      ////        0041  PAL  C   RSP  025-075  III/1
4060        A0116      ////      A1226  HOL  3   DSF  N39W23    7
3930        0120    0120        0120  LEA  G   RBR  245      110
3940        0205      ////        0205  PAL  C   RSP  075-180  III/1
3950        0207    0207        0207  LEA  U   RBR  245      240
3960        0546    0606        0635  G15  5   XRA  1-8A     C1.6  4.5E-03  2367
3960 +      B0548    U0558      A0653  SVI  2   FLA  S19E04    1F     ERU     2367
4280        0654      ////        0739  LEA  U   RSP  025-037  VI/1
3970        0706    0706        0706  LEA  G   RBR  245      120

```

Figure 5: Sample Space Weather Report text file from June 6, 2015. Along with event types and times, the reports also contain information about event locations, frequencies, and additional classification details. The relevant columns for this project are the “Begin” and “End” columns which denote the start and end times of events in UTC, where a time of 2:45 PM UTC would be presented as 1445 in the table. The “Obs” column denotes the observatory or satellite which observed the event in question. All XRA events are measured using the GOES satellites to determine an increase in X-Ray flux at the Earth.

## Data Wrangling

In order to generate our testing, training and validation data sets we have written Python scripts which utilize the space weather reports and the SUNPY Python package to download and store AIA observations. These scripts download one observation per event per wavelength, for a specified event type and set of wavelengths, which are chosen at random from all the observations taken over the duration of each event which fit the specified parameters.

The primary challenge we faced was managing the sheer quantity of data, requiring high-throughput computing. Each image, stored as a FITS file, is 12 MB in size, and we have approximately 60,000 observed events. This means that a full collection of images would require almost a full terabyte of storage space per wavelength. To use a local machine would require slowly downloading several terabytes of data using the SUNPY package, which takes about 30 seconds to retrieve a single FITS image. Acquiring 60,000 images in three wavelengths would then take roughly two months of download time. This would also require 3 terabytes of hard drive space, all of which would need to be continually stored and removed from memory while training our machine learning models.

To address these storage, speed, and memory concerns, we were able to utilize somewhat atyp-

ical resources for high-throughput computing: Google Drive and Google Colaboratory (shortened to Colab). As Rice students, we received unlimited Google Drive storage in our shared drive, allowing us to solve the storage issue. Google Colab is well-integrated with Google Drive, allowing us to directly access files stored in Drive using a Colab notebook without any additional local storage steps. Google Colab also allowed each member to run a separate instance of our downloading routine in a separate notebook, which was further aided by two instances running on the fried.rice.edu machine managed by our advisor. This produced a factor of six increase in downloading speed, shortening the two-month requirement to only ten days.

The main challenge when using Google Colaboratory was the memory requirement. Colab notebooks are limited to about 25 GB of RAM, which was not enough to train our models on more than a handful of images at a time when using full-size or even somewhat downsized images. The high resolution of each image ( $4096 \times 4096$  pixels) makes the files unreasonably large to be used in our convolutional neural networks (CNNs), described in the Methods & Models section. Large images require larger neural net architectures, dramatically increasing the memory requirement and slowing the training process. To remedy these challenges, we produced compressed and downsampled ( $8\times$ ) versions of our downloaded images in the .gz format for use in training and testing our models. This allowed us to train our models under the 25 GB RAM requirement put forth by Google Colaboratory, alongside the memory-conserving process of training in batches using checkpoints. With these improvements, we were able to train models in batches of 750 at a time.

The down sampling is performed as a mean pool on  $8 \times 8$  arrays of pixels, reducing the resolution to  $512 \times 512$  pixels, and reducing the file size to about 1 MB. A resolution of  $512 \times 512$  pixels was chosen for two primary reasons. The first is that  $512 \times 512$  is the lowest resolution where we believe the relevant features on the Sun, the flares that we see, retain significant detail. The difference between the two different down sampling resolutions we considered,  $512 \times 512$  and  $1024 \times 1024$ , is shown in Figure 6.

CNN architecture is optimized for input values between zero and one. Although our models were able to run using unnormalized images, we chose to normalize our images for several reasons. One concern is that the model could potentially adjust its weights such that it searches only for brighter XRA events and ignores the dimmer events. Some events on the Sun can be so bright that a handful of pixels are orders of magnitude brighter than the rest of the Sun, making it difficult for our CNNs to learn, because bright peaks in the EUV will not necessarily originate from X-ray flares. By logarithmically normalizing our images, our CNN models are better able to make determinations and classifications based on the features seen on the surface of the Sun, as shown in Figure 11. The loss metric is also more consistent between batches when training on normalized images. Several normalization functions were tested, and the final function used is shown below in Equation 1,

$$n(x) = 1 - \exp\left(-\frac{x}{10\tilde{\mu}}\right) \quad (1)$$

where  $x$  is the initial pixel value and  $\tilde{\mu}$  denotes the median pixel value of the image. Our normalization function rescales each pixel value,  $x$ , from  $[0, \infty)$  to  $[0, 1)$ . The median pixel value is a robust statistic expected to be roughly consistent across images. An example of this normalization is shown in Figure 7.



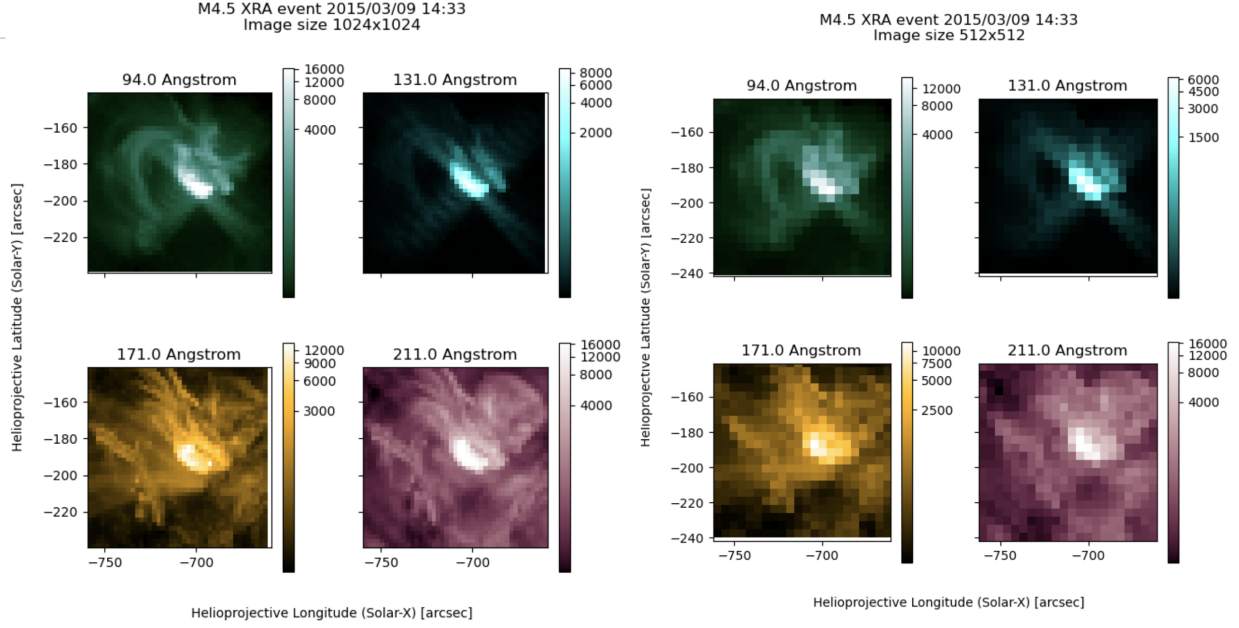


Figure 6: Resolution Comparison For A Solar Flare Feature. Left: A  $1024 \times 1024$  downsampled image of a solar event. Right: A  $512 \times 512$  downsampled image of the same solar event. Fine details are lost with downscaling, although the general structure is retained.

## Exploratory Data Analysis & Visualization

While exploring the space weather reports we have found 79.6% of the reports since 2010 have at least one observed space weather event, and there are on average 15.0 events per day. There are significant frequency discrepancies between the different types of space weather events. As shown in Figure 4, the most common events are X-ray events (XRA), optical flares in H-Alpha (FLA), Sweep-Frequency Radio Bursts (RSP), and Fixed-Frequency Radio Bursts (RBR). Each of these events comprise almost a quarter of the dataset. Because each of these four weather types have thousands of observed events to use and the remaining types have at most hundreds of observed events, we have decided to focus primarily on these four types of events for this project.

Another key feature that we have identified in the data is the typical size of a visible space weather event. Most flares and prominences are on the order of about 100 pixels in each dimension, as shown in Figure 8. This is good because it should allow us to down sample our images considerably from their original size of  $4096 \times 4096$  pixels, which would be challenging to run through a CNN.

## Methods & Models

To achieve our goal of identifying solar events from AIA images, we used convolutional neural networks (CNNs) using Keras in a Python environment. Because the size of the solar events in the AIA data is less than a percent of the full image, existing image identification CNN architecture could not be used to identify these solar events. Most existing image classification CNNs classify features which comprise a majority of the image, and as such are able to downsize the input images.

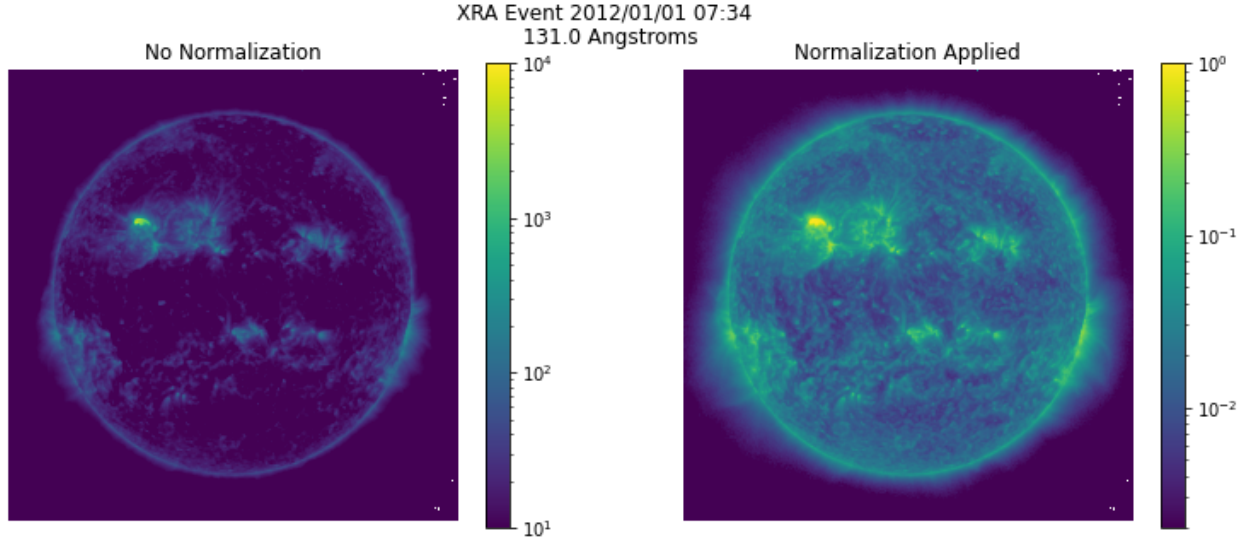


Figure 7: A typical solar image at  $131\text{\AA}$  when an X-ray flare is present. On the left is the image before normalization. On the right is the image after normalization. Both these images are plotted on a logarithmic scale. In the normalized image, the large peaks in brightness are retained, but the remaining parts of the solar surface are not as comparatively dim as in the non-normalized image.

When using a lower sized image, the CNN is able to train on images more quickly than for larger images. When attempting to train using the full  $4096 \times 4096$  AIA images, we found that Keras would use exorbitant amounts of memory in the training process. After downsizing the images by a factor of four to  $1024 \times 1024$  pixels, we found that even a simple model required over three hours to train on a set of 400 images, which is less than a tenth of our dataset. We also found that the validation accuracy obtained for these models were approximately 50% when training on 400 images. Due to hardware limitations, primarily in memory and speed, we chose to train our models using AIA images downsized by a factor of eight to a resolution of  $512 \times 512$  pixels. Although there could be some lost detail in the downsized images, the events still retain some visible structure at this resolution as shown in Figure 3. Additionally, our models using  $512 \times 512$  pixel images were able to train on a dataset containing four thousand images over four epochs in the same time a model would require to train on four hundred images using the  $1024 \times 1024$  pixel images.

Our final model takes a stack of three different wavelength  $512 \times 512$  pixel images as its input, then runs the images through three layers of convolution and maxpooling. The convolution layers are the crucial components of the CNN—these are the convolutional kernels whose weights are determined in order to identify image features. These kernels iterate through each image, and adjust their weights to better identify the image features with the goal of producing the desired output (whether an XRA event is present in an image or not). Multiple kernels are optimized in each layer to increase the number of “channels,” allowing more types of features to be identified. After each convolution is a maxpool layer, which reduces the size of the image by grouping boxes of pixels together and setting the resulting combined pixel value as the highest of the grouped pixels’ values. The resulting 3-dimensional structure is then flattened and run through a dense layer to output a single value between 0 and 1. If this value is greater than 0.5, the image is labeled as having a flare. This structure is shown in Figure 9.

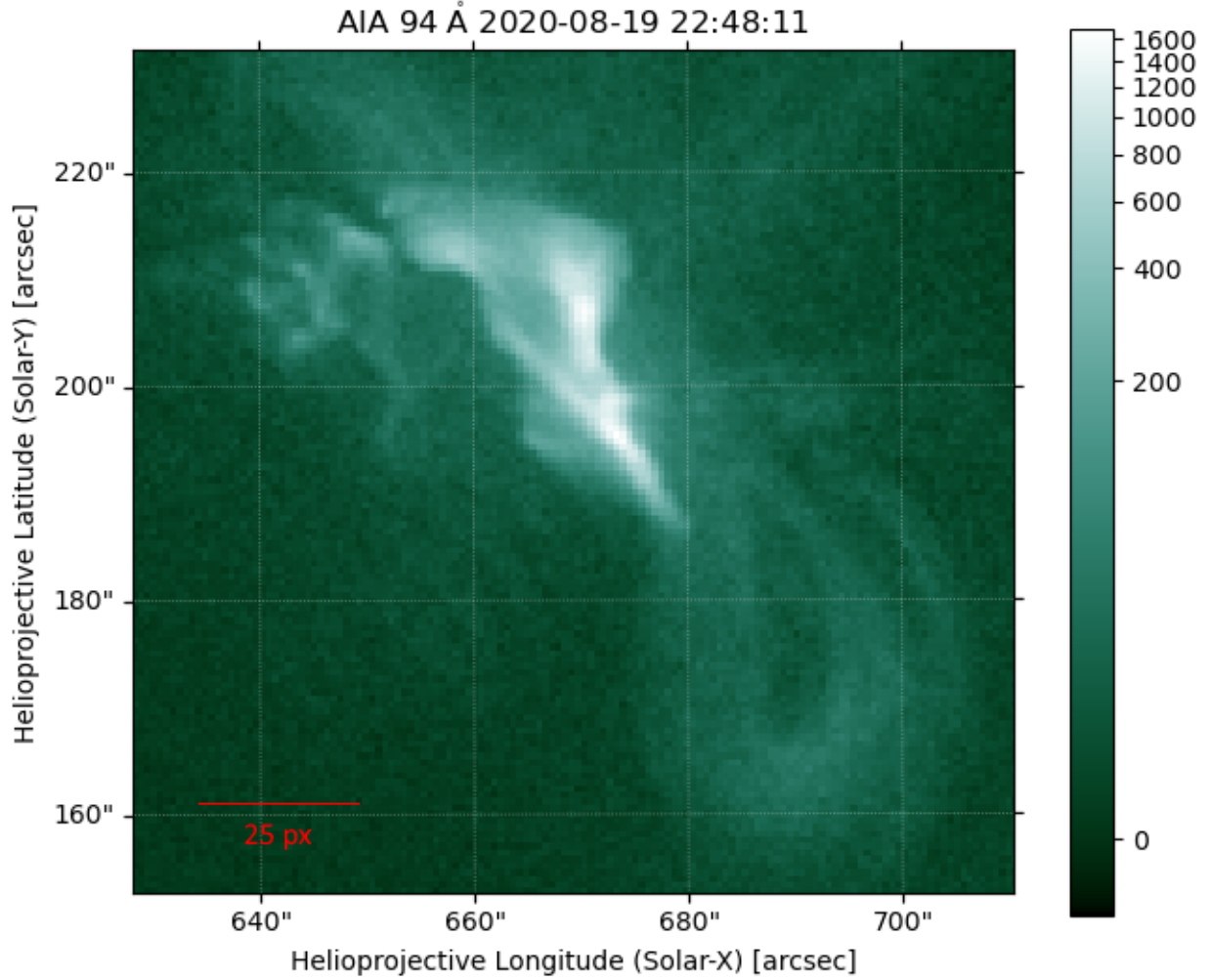


Figure 8: Typical scale for an X-ray flare. Captured in the 94 Å wavelength taken on August 8, 2020 at 10:48 UST. This image is shown in the full 4096×4096 resolution of AIA images. One arcsecond on the Sun’s surface is approximately 700km, so the red scale bar in this image is about 18,000km across

Our main metric used to measure the effectiveness of a certain model was the validation accuracy, with other secondary factors taken into consideration such as the speed or memory usage of a model. When training our models, we also aimed to reduce overfitting, which occurs when the validation loss is significantly higher than the training loss. Overfitting is a sign that the model is fitting too closely to the training dataset, and not identifying the structure of the desired features.

Conceptually, a single layer neural network would be effective if there are a limited number of ways that an event can appear in our data. In contrast, a multi-layer or deep learning model would build up the structure of features across several layers, which results in more insight into the structure of various events. We find that our models do perform better with more layers, as shown in Figures 12 and 13. An additional parameter considered when creating model structures was the number of wavelengths used. Different wavelengths are able to analyze different layers in the atmosphere of the Sun, and therefore different structure in solar events. Through the use of

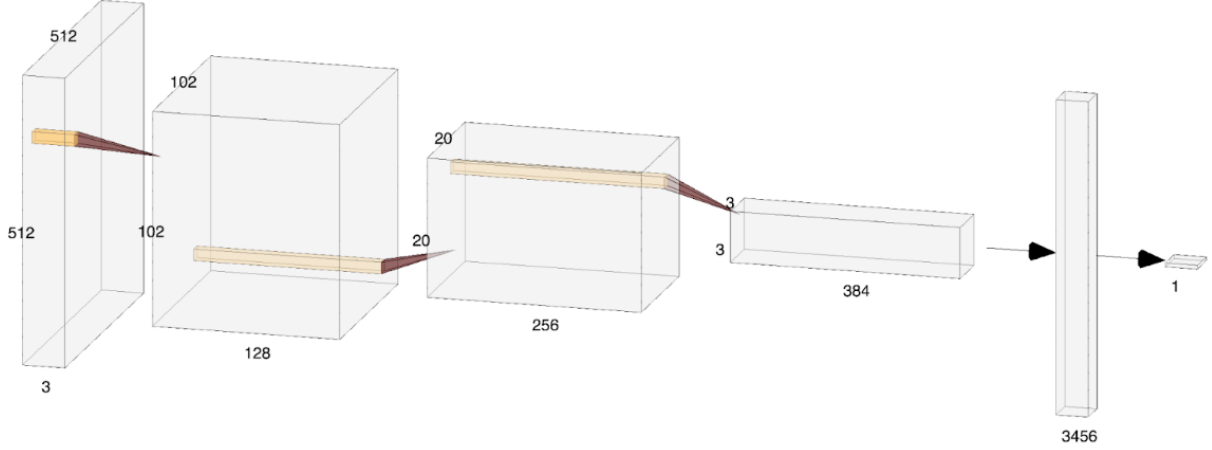


Figure 9: The architecture of our final CNN. The initial inputs are images sized  $512 \times 512$  pixels in three wavelengths which are then subject to three convolution and pooling layers, and then are flattened to obtain a final decimal output indicating the probability that an event is present. In this graphic of our CNN architecture, the number of channels in a specific layer is marked at the bottom and the other axes are the array size.

images in multiple wavelengths, a model can better identify events by incorporating features from all wavelengths used.

## Results

For both single wavelength images, as well as multi-wavelength images, we find that the “deep-learning” CNN models, perform significantly better than simple single or two-convolution layer models. The deep-learning CNN models, which contain at least three layers of convolutions and max-pooling, take longer to over fit and reach higher validation accuracy values. This is demonstrated in Figure 12, which uses a two convolution layer model trained on  $171 \text{ \AA}$  and Figure 13 which uses three convolution layers.

XRA events do appear to carry some signature visible to a neural network that distinguish them from other types of events or non-events likely held within the multiple wavelength information. 65-75% validation accuracy is possible with single-wavelength models, but this is improved when applying multiple wavelengths.

One possible reason for the higher multi-wavelength accuracy is that, because XRA events emit light predominantly in the X-ray, XRA events will have a higher intensity at bluer wavelengths than redder wavelengths. In contrast, the Sun’s peak wavelength is in the optical, so in the ultraviolet wavelength range, bluer wavelengths will have a weaker intensity than redder wavelengths. This suggests that X-ray events would have a different intensity relationship with wavelength than the background surface of the Sun, which the neural network could be using to identify these events. If this is the case, then optical flares may be more difficult to identify, as this inverted relationship does not hold for an event peaking in the optical.

Our final three wavelength, three layer model was able to achieve training and validation accuracies of 75-80% when trained on over 6000 images, and an accuracy of 70% on a final testing

dataset, separate from the training dataset. The performance of this model is shown in Figure 10. These results indicate that our model is able to accurately identify the presence of an X-ray flare using only images of the Sun in EUV wavelengths with an accuracy of almost 80%.

## Conclusion & Future Work

From our results, we have established that solar X-ray events can be reliably identified from images of the Sun in the ultraviolet wavebands using convolutional neural networks. This serves as a proof of concept for future work in predicting these X-ray events using EUV images of the Sun. Because X-ray flares have an increased intensity in the EUV during the preflare phase, as shown in Figure 1, it would be informative to train a CNN to identify these events before the impulsive X-ray phase of the event occurs. Since we have shown that EUV images can be used to identify X-ray flares during the event, we believe it should be possible to identify them during the preflare phase as well. This ability would be useful in providing a warning—if only by a few minutes—of the onset of more dangerous X-ray radiation, allowing time to implement protections for astronauts or electronics systems.

A natural extension of this work would be a multiclass, multi-label classifier for all 15 SWPC categories of solar events, ideally using all 10 AIA wavelengths. A multi-label classifier would be able to handle overlapping solar events, which likely take up a non-negligible portion of the data set. Alternative methods avoiding the use of convolutional neural nets, such as spectral index analysis or applying simple intensity thresholds may also be able to produce good results. Attempting to isolate which features our models are using to classify these events may also prove fruitful.

## Software

Our project was coded entirely in Python using our homemade ABWOC (Astros But WithOut Cheating) package, which is available at <https://github.com/PHYS477677/abwoc>.

## References

- [1] Trudy E. Bell and Tony Philips. A Super Solar Flare. 2008.
- [2] National Research Council. *Severe Space Weather Events: Understanding Societal and Economic Impacts: A Workshop Report*. Washington, DC: The National Academies Press, 2008.
- [3] Bradley W. Carroll and Dale A. Ostlie. *An Introduction to Modern Astrophysics*. Cambridge University Press, 2 edition, 2017.
- [4] J. Dai, Q. M. Zhang, Y. N. Su, and H. S. Ji. Transverse oscillation of a coronal loop induced by a flare-related jet. *Astronomy & Astrophysics*, 646:A12, February 2021.
- [5] L. P. Chitta, H. Peter, and S. K. Solanki. Nature of the energy source powering solar coronal loops driven by nanoflares. *Astronomy & Astrophysics*, 615:L9, July 2018.

- [6] Markus J. Aschwanden and Hardi Peter. The Width Distribution of Loops and Strands in the Solar Corona—Are We Hitting Rock Bottom? *The Astrophysical Journal*, 840(1):4, May 2017.
- [7] Abbas Raboonik, Hossein Safari, Nasibe Alipour, and Michael Wheatland. Prediction of solar flares using unique signatures of magnetic field images. *The Astrophysical Journal*, 834, 10 2016.
- [8] Arnold Benz. Flare observations. *Living Reviews in Solar Physics*, 5, December 2008.
- [9] W. Dean Pesnell, B. J. Thompson, and P. C. Chamberlin. The Solar Dynamics Observatory (SDO). *Solar Physics*, 275(1-2):3–15, January 2012.
- [10] Conceptual Image Lab NASA, Goddard Space Flight Center. Solar dynamics observatory - concept, 2008.
- [11] AIA Science Team. Atmospheric Imaging Assembly for the Solar Dynamics Observatory, Concept Study Report, Appendix A (AIA Science Plan) . Feb. 2004.
- [12] D. C. Wells, E. W. Greisen, and R. H. Harten. FITS - a Flexible Image Transport System. *Astronomy and Astrophysics Supplement*, 44:363, June 1981.
- [13] Stuart J. Mumford, Nabil Freij, Steven Christe, Jack Ireland, Florian Mayer, Albert Y. Shih, David Stansby, V. Keith Hughitt, Daniel F. Ryan, Simon Liedtke, David Pérez-Suárez, Vishnunarayan K I., Laura Hayes, Pritish Chakraborty, Andrew Inglis, Punyaslok Pattnaik, Brigitta Sipőcz, Rishabh Sharma, Andrew Leonard, Russell Hewett, Alex Hamilton, Abhijeet Manhas, Asish Panda, Matt Earnshaw, Will Barnes, Nitin Choudhary, Ankit Kumar, Raahul Singh, Prateek Chanda, Md Akramul Haque, Michael S Kirk, Michael Mueller, Sudarshan Konge, Rajul Srivastava, Yash Jain, Samuel Bennett, Ankit Baruah, Quinn Arbolante, Michael Charlton, Sashank Mishra, Shane Maloney, Nicky Chorley, Himanshu, Aryan Chouhan, James Paul Mason, Sanskar Modi, Yash Sharma, Lazar Zivadinovic, Naman9639, Jose Ivan Campos Rozo, Larry Manley, Monica G. Bobra, Agneet Chatterjee, Kateryna Ivashkiv, Johan Freiherr von Forstner, Juanjo Bazán, Kris Akira Stern, John Evans, Sarthak Jain, Michael Malocha, Sourav Ghosh, Airmansmith97, Dominik Stańczak, Rajiv Ranjan Singh, Ruben De Visscher, Shresth Verma, SophieLemos, Ankit Agrawal, Arib Alam, Dumindu Buddhika, Himanshu Pathak, Jai Ram Rideout, Swapnil Sharma, Jongyeob Park, Matt Bates, Pankaj Mishra, Deepankar Sharma, Dhruv Goel, Garrison Taylor, Goran Cetusic, Guntbert Reiter, Jacob, Mateo Inchaurrendieta, Sally Dacie, Sanjeev Dubey, Arthur Eigenbrot, Erik M. Bray, Jeffrey Aaron Paul, Rutuja Surve, Serge Zahniy, Sudeep Sidhu, Tomas Meszaros, Utkarsh Parkhi, Abhigyan Bose, Abhishek Pandey, Adrian Price-Whelan, Amogh J, André Chicrala, Ankit, Chloé Guennou, Daniel D’Avella, Daniel Williams, Dipanshu Verma, Jordan Ballew, Nick Murphy, Priyank Lodha, Thomas Robitaille, Tom Augspurger, Yash Krishan, honey, neerajkulk, Andrew Hill, Benjamin Mampaey, Bernhard M. Wiedemann, Carlos Molina, Duygu Keşkek, Ishtyaq Habib, Joseph Letts, Ole Streicher, Reid Gomillion, Yash Kothari, mridulpandey, Abigail L. Stevens, Abijith B, Abijith Bahuleyan, Ambar Mehrotra, Arfon Smith, Arseniy Kustov, Brandon Stone, Conor MacBride, Emmanuel Arias, Erik Tollerud, Fionnlagh Mackenzie Dover, Freek Verstringe, Gulshan Kumar,



- Harsh Mathur, Igor Babuschkin, James Calixto, Jaylen Wimbish, Juan Camilo Buitrago-Casas, Kalpesh Krishna, Kaustubh Hiware, Koustav Ghosh, Kritika Ranjan, Manas Mangonkar, Mark Cheung, Matthew Mendero, Mickaël Schoentgen, Norbert G Gyenge, Rajasekhar Reddy Mekala, Rishabh Mishra, Shashank Srikanth, Shubham Jain, Swapnil Kanonjia, Tannmay Yadav, Tathagata Paul, Tessa D. Wilkinson, Thomas A Caswell, Tiago M. D. Pereira, Trung Kien Dang, Yudhik Agrawal, nakul shahdadpuri, platipo, resakra, yasintoda, and Sophie A. Murray. Sunpy, April 2021.
- [14] The SunPy Community, Will T. Barnes, Monica G. Bobra, Steven D. Christe, Nabil Freij, Laura A. Hayes, Jack Ireland, Stuart Mumford, David Perez-Suarez, Daniel F. Ryan, Albert Y. Shih, Prateek Chanda, Kolja Glogowski, Russell Hewett, V. Keith Hughitt, Andrew Hill, Kaustubh Hiware, Andrew Inglis, Michael S. F. Kirk, Sudarshan Konge, James Paul Mason, Shane Anthony Maloney, Sophie A. Murray, Asish Panda, Jongyeob Park, Tiago M. D. Pereira, Kevin Reardon, Sabrina Savage, Brigitta M. Sipőcz, David Stansby, Yash Jain, Garrison Taylor, Tannmay Yadav, Rajul, and Trung Kien Dang. The sunpy project: Open source development and status of the version 1.0 core package. *The Astrophysical Journal*, 890:68–, 2020.
- [15] J.R. Lemen, A.M. Title, and D.J. et al. Akin. The atmospheric imaging assembly (aia) on the solar dynamics observatory (sdo). *Solar Physics*, 275:17–40, January 2012.
- [16] Holly Zell. How sdo sees the sun. <https://www.nasa.gov/content/goddard/how-sdo-sees-the-sun/>, Feb 2015.
- [17] Users guide to the preliminary report and forecast of solar geophysical data. [https://www.swpc.noaa.gov/sites/default/files/images/u2/Usr\\_guide.pdf](https://www.swpc.noaa.gov/sites/default/files/images/u2/Usr_guide.pdf), Aug 2012.
- [18] NOAA. Space weather glossary. <https://www.swpc.noaa.gov/content/space-weather-glossary>.

## Appendix

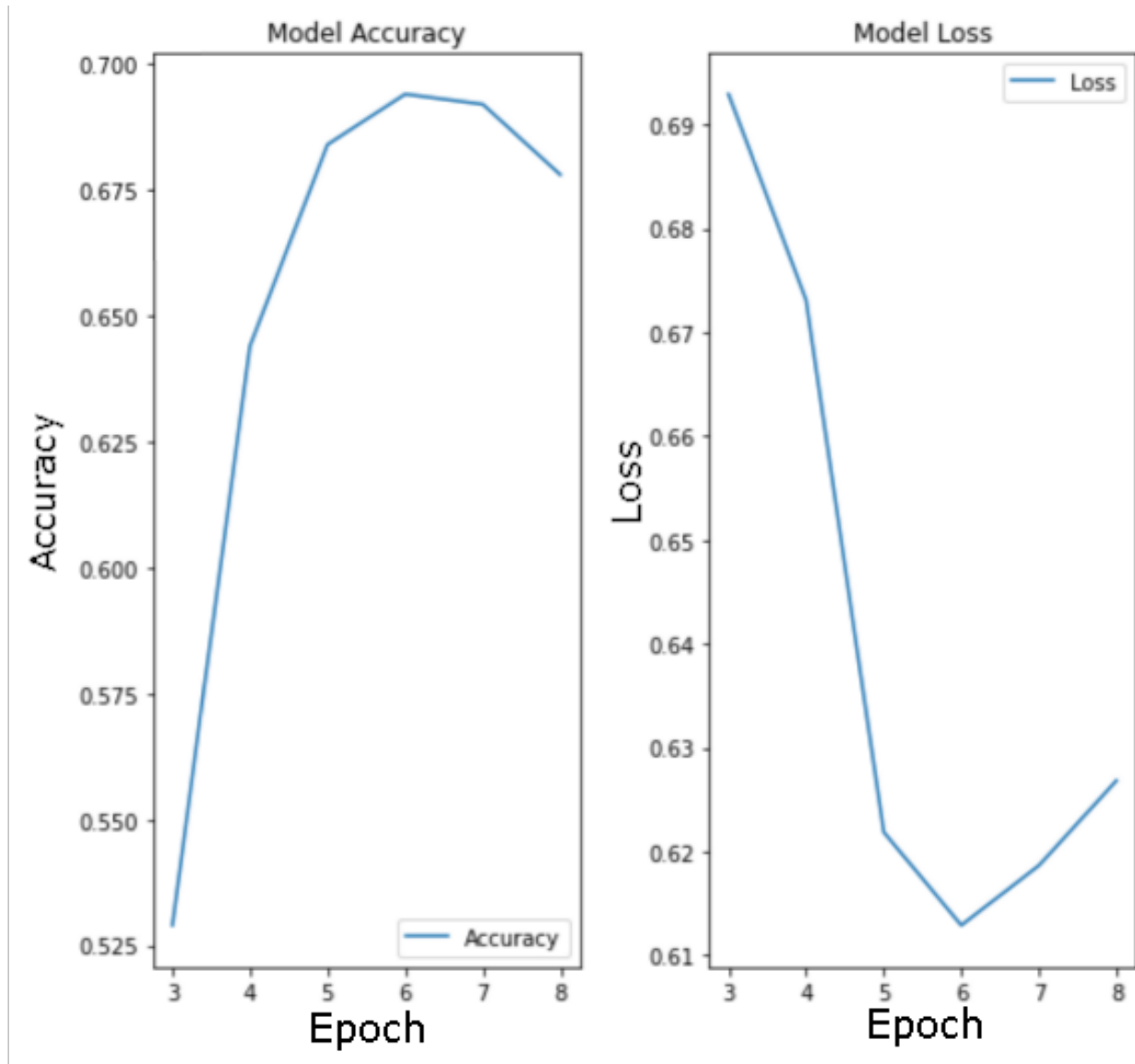


Figure 10: The performance of the final model, evaluated on a testing dataset using weights saved from the last several iterations of model training. The highest accuracy and lowest loss for this model both occur in the sixth epoch presented in this plot.

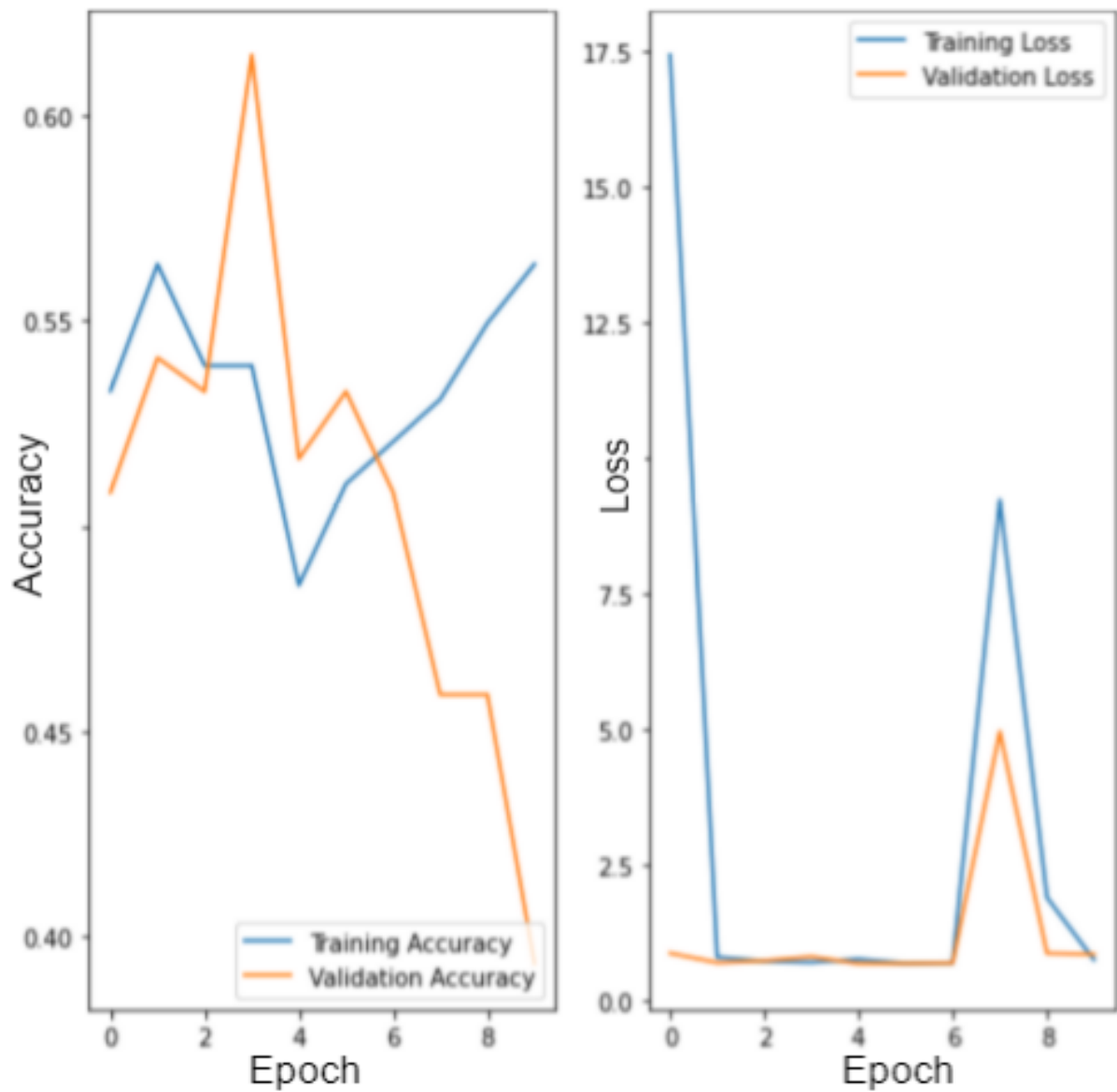


Figure 11: Model trained using images without our normalization function applied. The validation accuracy does not converge and the loss metrics are very sporadic, with a large range of loss values. This is an indicator that training our models without a normalization applied produces worse results than training a model using normalized images.

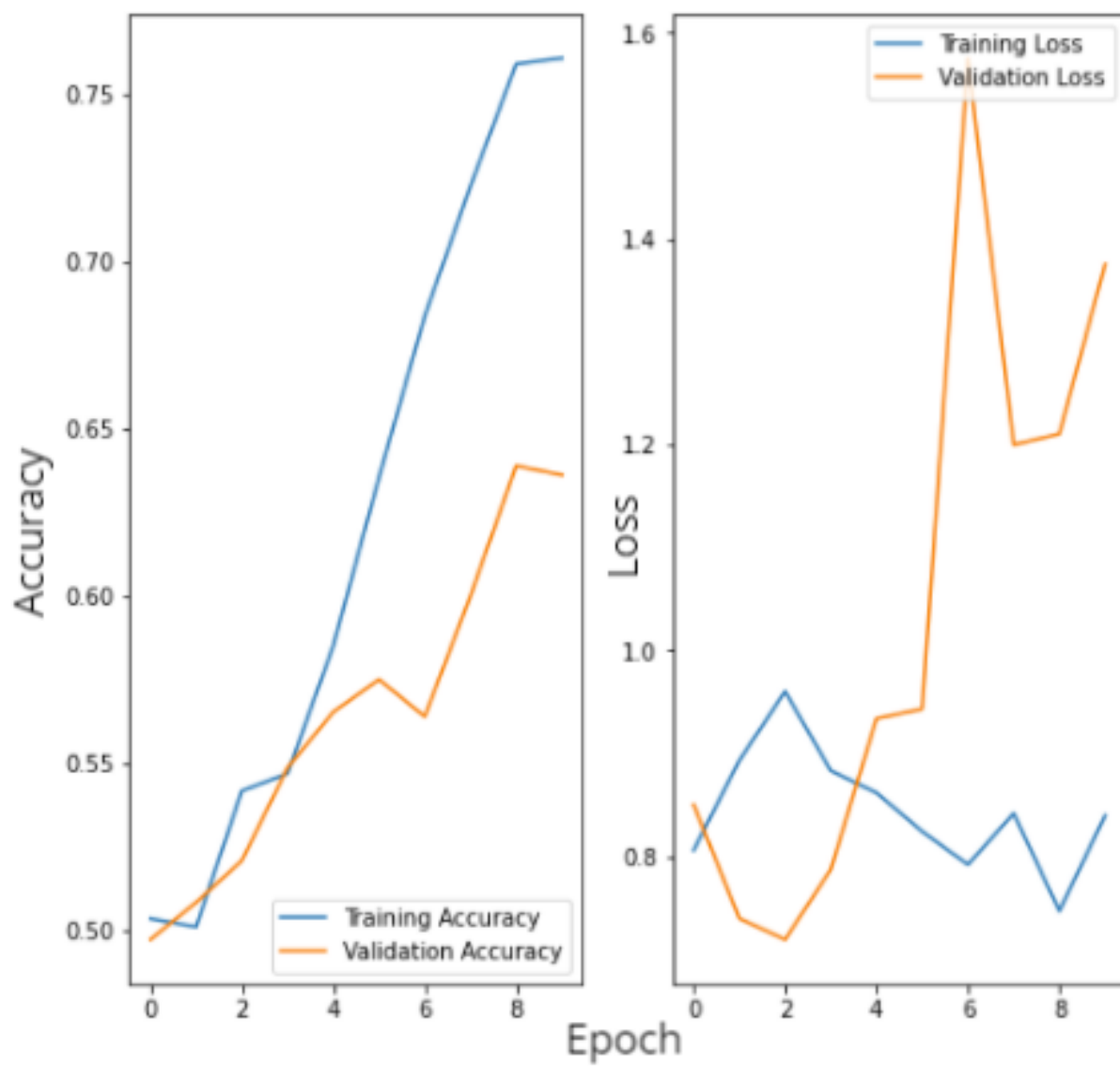


Figure 12: Model with two convolution layers trained using images in the 171 Å wavelength.

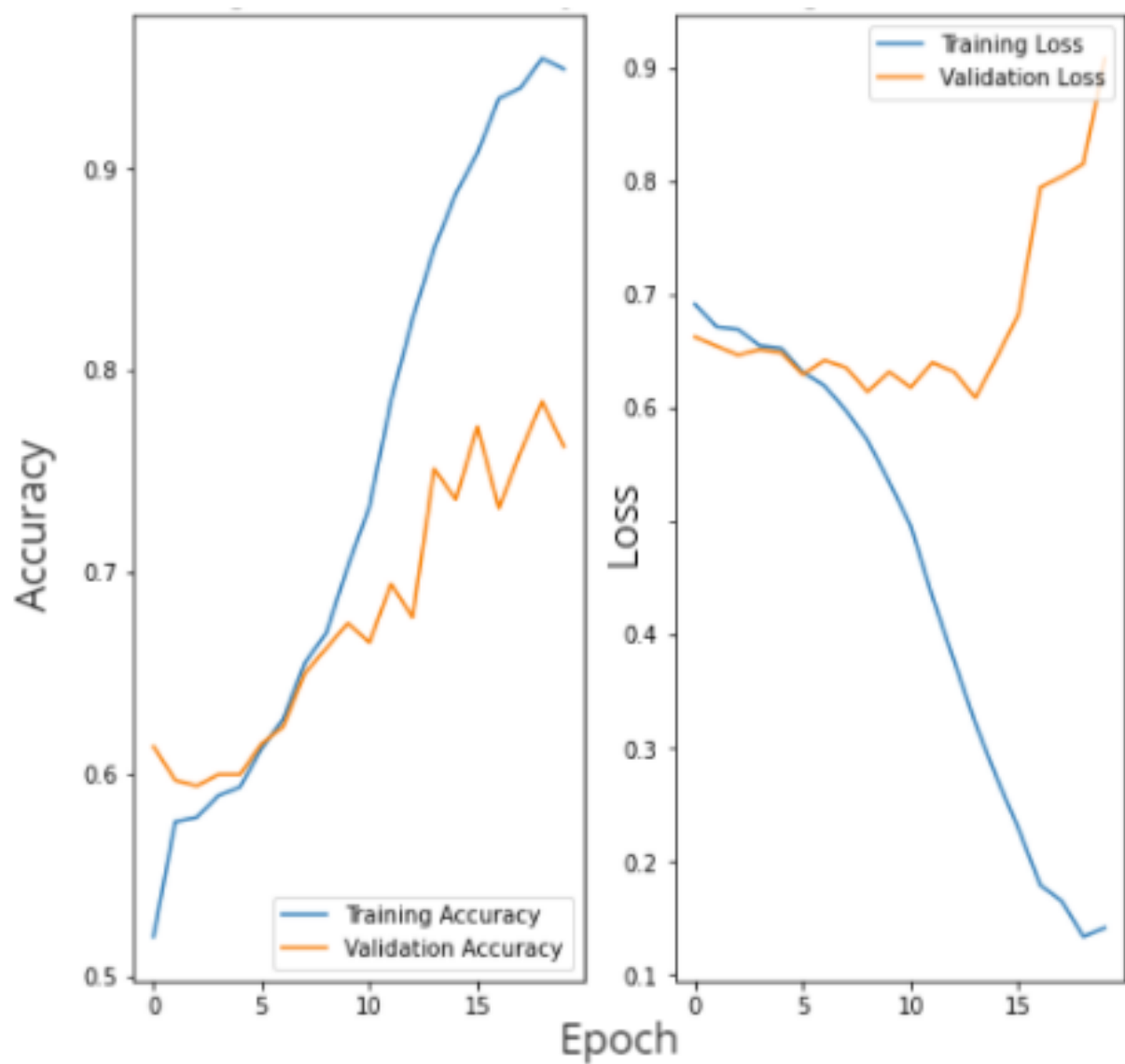


Figure 13: Model with three convolution layers trained using images in the 171 Å wavelength. This model results in higher accuracies and also takes longer to overfit than models with fewer layers.

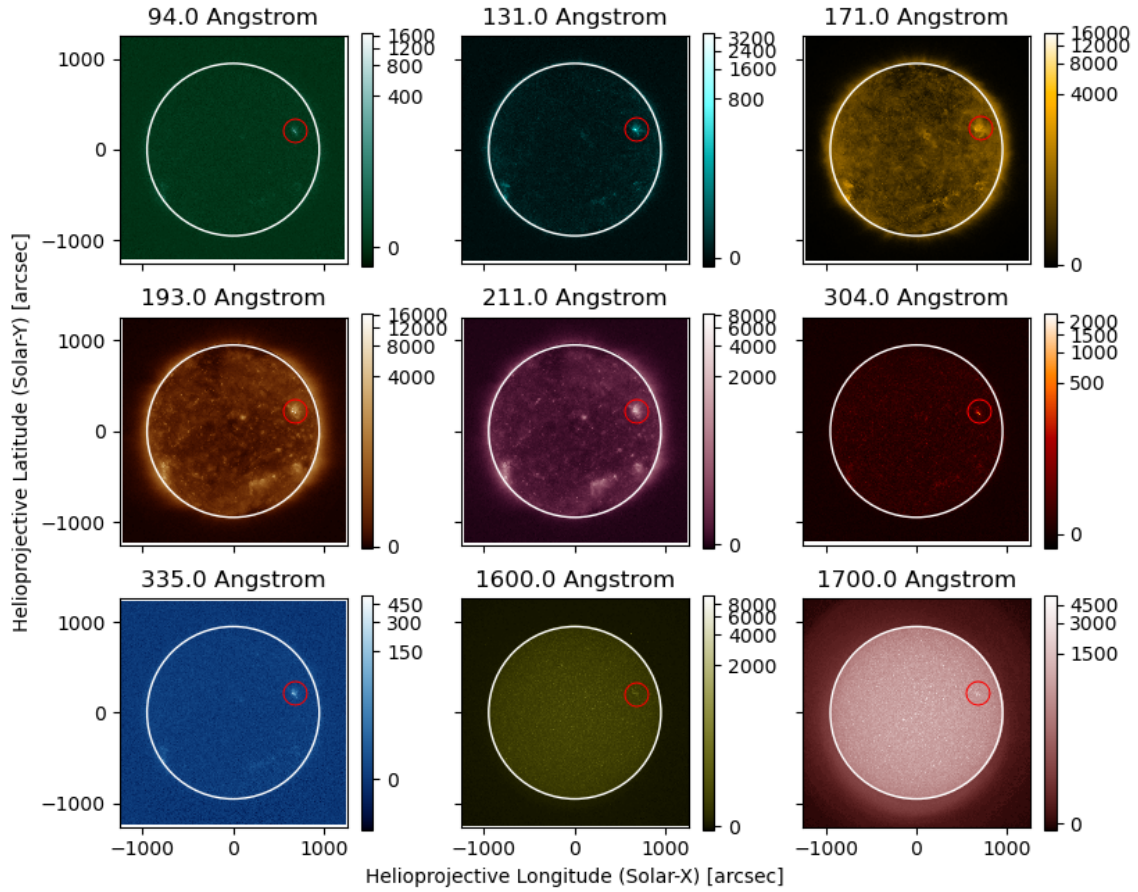


Figure 14: A small X-ray flare which occurred August 19, 2020 in each AIA wavelength apart from 4500 Å. The flare, circled in red on each image, shows up in all wavelengths to varying degrees.



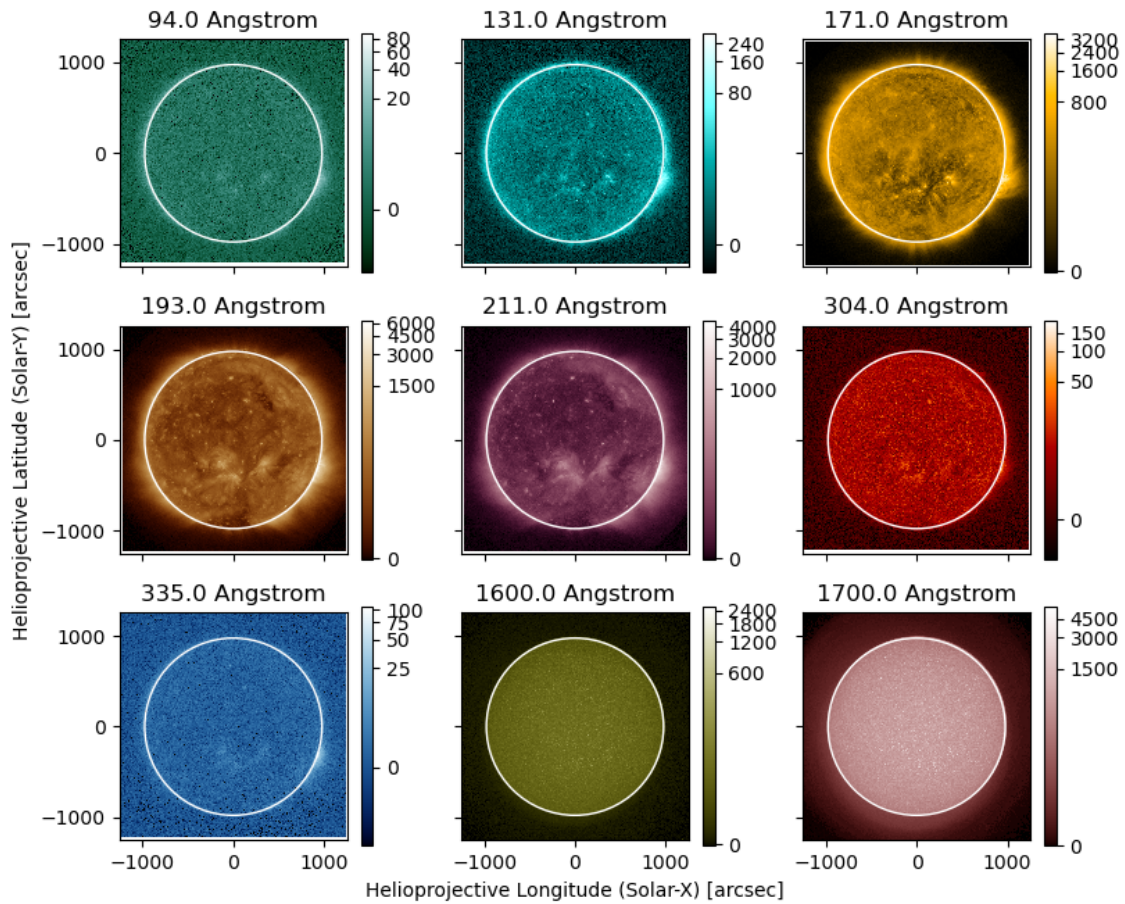


Figure 15: The Sun in each wavelength without an active flare. Note the much smaller colorbar scales than in the image above.